

Generalised Adaptive Cross Approximation for Convolution Quadrature based Boundary Element Formulation

A.M. Haider¹, S. Rjasanow², and M. Schanz¹

¹*Institute of Applied Mechanics, Graz University of Technology, Technikerstraße 4/II, 8010 Graz, Austria, m.schanz@tugraz.at*

²*Department of Mathematics, Saarland University, 66041 Saarbrücken, Germany, rjasanow@num.uni-sb.de*

Abstract

The acoustic wave equation is solved in time domain with a boundary element formulation. The time discretisation is performed with the generalised convolution quadrature method and for the spatial approximation standard lowest order elements are used. Collocation and Galerkin methods are applied. In the interest of increasing the efficiency of the boundary element method, a low-rank approximation such as the adaptive cross approximation (ACA) is carried out. We discuss about a generalisation of the ACA to approximate a three-dimensional array of data, i.e., usual boundary element matrices at several complex frequencies. This method is used within the generalised convolution quadrature (gCQ) method to obtain a real time domain formulation. The behaviour of the proposed method is studied with three examples, a unit cube, a unit cube with a reentrant corner, and a unit ball. The properties of the method are preserved in the data sparse representation and a significant reduction in storage is obtained.

Keywords: wave equation; boundary element method; generalised convolution quadrature; multivariate adaptive cross approximation

1 Introduction

Wave propagation problems appear often in engineering, e.g., for non-destructive testing or exploring the underground. Any of such problems are formulated with hyperbolic partial differential equations, e.g., in acoustics or elastodynamics. Sometimes the physical model allows to have a description with parabolic partial differential equations, e.g., for thermal problems. Despite that mostly a linear theory is sufficient, the handling of space and time requires expensive discretisation methods and for scattering problems even an unbounded domain has to be considered.

There are several numerical methods for solving such space and time dependent problems. Methods exist based on finite differences for both variables, as well as finite element methods in space in combination with finite differences in time or discontinuous Galerkin methods. These domain-based methods are often very efficient but have difficulties to handle unbounded domains, e.g., for scattering problems. The main problem is to truncate the computational domain with some approximations of the radiation condition. Especially for the latter class of problems, time domain boundary element methods (BEM) are a well established alternative because they inherently fulfil the radiation condition. The basis are boundary integral equations by the use of retarded potentials as counterpart to the governing hyperbolic partial differential equation. The mathematical theory goes back to the beginning of the last century by

Fredholm for scalar problems like acoustics and later by Kupradze [18] for vectorial problems in elasticity. The mathematical background of time-dependent boundary integral equations is summarised by Costabel [10] and extensively discussed in the textbook by Sayas [33].

The first numerical realisation of a time domain boundary element formulation is originated by Mansur [25] in the 80th of the last century. Despite often used, this approach suffers from instabilities (see, e.g., [30]). A stable space-time formulation has been published by Bamberger and Ha-Duong [3], which has been further explored by the group of Aimi [1, 2]. These approaches work directly in time domain, whereas a transformation to Laplace- or Fourier-domain results in suitable formulations [11] as well. These formulations in transformed domains have the advantage of being efficient from a memory point of view, since only elliptic problems have to be solved, which are of the size of one time step of the time-domain methods. However, to obtain the time-dependent solution several frequency-dependent solutions have to be computed, which are difficult to be solved with iterative solvers, especially for higher frequencies. Furthermore, suitable and mostly not physically motivated parameter choices have to be found for the inverse transformation technique. In contrast, the time-domain methods require a huge amount of memory since the matrices have to be stored for each time step (up to a cut-off in 3D). Somehow in between transformation and time-domain methods are BE formulations based on the convolution quadrature (CQ) method proposed by Lubich [23, 24]. Such a formulation is a true time stepping method utilising the Laplace domain fundamental solutions and properties. Applications of the CQ to BEM can be found, e.g., in [34, 36]. The generalisation of this seminal technique to variable time step sizes has been proposed by López-Fernández and Sauter [20, 22] and is called generalised convolution quadrature method (gCQ). Applications can be found in acoustics with absorbing boundary conditions [32] and in thermoelasticity [19]. A comparison of a transformation and a CQ based BEM can be found in [38].

The drawback of all BE formulations either for elliptic and much stronger for hyperbolic problems is the high storage and computing time demand as a standard formulation scales with $\mathcal{O}(M^2)$ for M unknowns. In time domain, additionally, the time complexity has to be considered, where in the case of a CQ based formulation the complexity is of order $\mathcal{O}(M^2N)$ for N time steps. For elliptic problems fast methods has been proposed as the fast multipole method (FMM) [17] or \mathcal{H} -matrix based methods with the adaptive cross approximation (ACA) used in the matrix blocks [8, 6]. For hyperbolic problems the extension of FMM to the time variable has been published in [15] for acoustics and in [41, 29] for elastodynamics. In combination with CQ, fast methods are published in combination with a reformulation of CQ. The CQ-algorithm can be rewritten such that several elliptic problems have to be solved [5, 35]. Based on this transformation the known techniques from the elliptic problems can be applied [4, 27].

Here, a different approach is used. Independently whether the CQ in the original form or gCQ is used, essentially, a three-dimensional data array has to be efficiently computed and stored. This data array is constructed by the spatial discretisation, resulting in two-dimensional data, and the used complex frequencies of the algorithm, which gives the third dimension. To find a low rank representation of this three-dimensional tensor the generalised adaptive cross approximation (3D-ACA) can be used. This technique is a generalisation of ACA [8] and is proposed by Bebendorf et al. [7, 9]. It is based on a Tucker decomposition [42] and can be traced back to the group of Tyrtshnikov [28]. The 3D-ACA might be seen as a higher-order singular value decomposition or as a multilinear SVD [12], which is a generalisation of the matrix SVD to tensors. An alternative but related approach is presented in [13]. This approach does not look for a low rank representation but uses an interpolation with respect to the frequencies to reduce the total amount of necessary frequencies to establish the time domain solution.

Here, the 3D-ACA is applied on a gCQ based time domain formulation utilising the original idea of the multivariate ACA [9]. Recently a very similar approach has been published by Seibel [39], where the conventional convolution quadrature method is used and, contrary to the approach proposed here, the \mathcal{H}^2 technique is used for the approximation of the boundary element matrices at the different frequencies.

2 Problem statement

Let $\Omega \subset \mathbb{R}^3$ be a bounded Lipschitz domain and $\Gamma = \partial\Omega$ its boundary with the outward normal \mathbf{n} . The acoustic wave propagation is governed by

$$\frac{\partial^2}{\partial t^2} u(\mathbf{x}, t) - c^2 \Delta u(\mathbf{x}, t) = 0 \quad (\mathbf{x}, t) \in \Omega \times (0, T) \quad (1)$$

$$u(\mathbf{x}, 0) = \frac{\partial}{\partial t} u(\mathbf{x}, 0) = 0 \quad \mathbf{x} \in \Omega \quad (2)$$

$$\gamma_0 u(\mathbf{x}, t) = g_D(\mathbf{x}, t) \quad (\mathbf{x}, t) \in \Gamma_D \times (0, T) \quad (3)$$

$$\gamma_1 u(\mathbf{x}, t) = g_N(\mathbf{x}, t) \quad (\mathbf{x}, t) \in \Gamma_N \times (0, T) \quad (4)$$

with the wave speed c and the end time $T > 0$. Γ_D and Γ_N denote either a Dirichlet or Neuman boundary. The respective traces are defined by

$$\gamma_0 u(\mathbf{x}, t) = \lim_{\Omega \ni \mathbf{x} \rightarrow \mathbf{x} \in \Gamma} u(\mathbf{x}, t) \quad (5)$$

for the Dirichlet trace and with

$$\gamma_{1,x} u(\mathbf{x}, t) = \lim_{\Omega \ni \mathbf{x} \rightarrow \mathbf{x} \in \Gamma} (\nabla u(\mathbf{x}, t) \cdot \mathbf{n}) = q(\mathbf{x}, t) \quad (6)$$

for the Neumann trace, also known as the conormal derivative or flux $q(\mathbf{x}, t)$.

The given problem can be solved with integral equations. Essentially, either an indirect approach using layer potentials or an direct approach are suitable. In the subsequent numerical tests both methodologies are used to show distinct features of the proposed method. First, the retarded boundary integral operators have to be formulated. It is the single layer potential

$$(\mathcal{V} * q)(\mathbf{x}, t) = \int_0^t \int_{\Gamma} \gamma_0 U(\mathbf{x} - \mathbf{y}, t - \tau) q(\mathbf{y}, \tau) \, d s_{\mathbf{y}} \, d \tau, \quad (7)$$

where the fundamental solution is $U(\mathbf{x} - \mathbf{y}, t - \tau) = \frac{1}{4\pi \|\mathbf{x} - \mathbf{y}\|} \delta\left(t - \tau - \frac{\|\mathbf{x} - \mathbf{y}\|}{c}\right)$ introducing a weak singularity. Here, $\delta(\cdot)$ denotes the Dirac distribution. The double layer potential is defined by

$$(\mathcal{K} * u)(\mathbf{x}, t) = \int_0^t \int_{\Gamma} \gamma_{1,y} U(\mathbf{x} - \mathbf{y}, t - \tau) u(\mathbf{y}, \tau) \, d s_{\mathbf{y}} \, d \tau \quad (8)$$

and its adjoint

$$(\mathcal{K}' * u)(\mathbf{x}, t) = \int_0^t \gamma_{1,x} \int_{\Gamma} U(\mathbf{x} - \mathbf{y}, t - \tau) u(\mathbf{y}, \tau) \, d s_{\mathbf{y}} \, d \tau. \quad (9)$$

The remaining operator to be defined is the hypersingular operator

$$(\mathcal{D} * u)(\mathbf{x}, t) = - \int_0^t \gamma_{1,x} \rlap{-}\int_{\Gamma} \gamma_{1,y} U(\mathbf{x} - \mathbf{y}, t - \tau) u(\mathbf{y}, \tau) \, d s_{\mathbf{y}} \, d \tau, \quad (10)$$

where $\rlap{-}\int$ indicates that this integral has to be defined in the sense of Hadamard. Using these operators, which are also called retarded potentials, the solution for the Dirichlet problem related to (1) can be obtained by

$$(\mathcal{V} * q)(\mathbf{x}, t) = \left(\mathcal{C} g_D + (\mathcal{K} * g_D) \right)(\mathbf{x}, t) \quad (\mathbf{x}, t) \in \Gamma_D \times (0, T) \quad (11)$$

with $\Gamma = \Gamma_D$. On the right hand side the so-called integral free term

$$\mathcal{C} g_D(\mathbf{x}, t) = \lim_{\varepsilon \rightarrow 0} \int_{\partial B_{\varepsilon}(\mathbf{x}) \cap \Omega} \nabla \frac{1}{\|\mathbf{x} - \mathbf{y}\|} \cdot \mathbf{n} g_D(\mathbf{y}, t) \, d s_{\mathbf{y}} + g_D(\mathbf{x}, t). \quad (12)$$

has to be considered with $B_\varepsilon(\mathbf{x})$ denoting a ball of radius ε centered at \mathbf{x} and $\partial B_\varepsilon(\mathbf{x})$ is its surface. In case of the Galerkin formulation this expression reduces to $1/2g_D(\mathbf{x},t)$ but in the collocation schema it is dependent on the geometry at the collocation node. See, e.g., [26] for a description how the integral free term depends on the geometry. Alternatively to (11), the indirect approach

$$(\mathcal{V} * \vartheta)(\mathbf{x},t) = g_D(\mathbf{x},t) \quad (\mathbf{x},t) \in \Gamma_D \times (0,T) \quad (13)$$

can be used, where $\vartheta(\mathbf{x},t)$ denotes the density function. The Neumann problem can be solved with the second boundary integral equation

$$(\mathcal{D} * u)(\mathbf{x},t) = - \left(\frac{1}{2} \mathcal{I} g_N - (\mathcal{K}' * g_N) \right)(\mathbf{x},t) \quad (\mathbf{x},t) \in \Gamma_N \times (0,T), \quad (14)$$

where the integral free term is already substituted by the expression holding only for the Galerkin approach. The hypersingular integral is reduced to a weak singular one by partial integration, see, e.g., [40].

3 Boundary element method: Discretisation

Spatial discretisation The boundary Γ is discretised with elements resulting in an approximation Γ^h which is the union of geometrical elements

$$\Gamma^h = \bigcup_{e=1}^E \tau_e. \quad (15)$$

τ_e denote boundary elements, here linear surface triangles, and their total number is E .

Next, finite element bases on boundaries Γ_D and Γ_N are used to construct the approximation spaces

$$X_D = \text{Span}\{\varphi_1, \varphi_2, \dots, \varphi_{M_1}\}, \quad (16)$$

$$X_N = \text{Span}\{\psi_1, \psi_2, \dots, \psi_{M_2}\}. \quad (17)$$

The unknowns u and q are approximated by a linear combination of functions in X_D and X_N

$$u^h = \sum_{\ell=1}^{M_1} u_\ell(t) \varphi_\ell(\mathbf{y}) \quad \text{and} \quad q^h = \sum_{k=1}^{M_2} q_k(t) \psi_k(\mathbf{y}) \quad \text{and} \quad \vartheta^h = \sum_{k=1}^{M_2} \vartheta_k(t) \psi_k(\mathbf{y}). \quad (18)$$

Note, the coefficients $u_\ell(t)$, $q_k(t)$, and $\vartheta_k(t)$ are still continuous functions of time t . In the following, the shape functions φ_ℓ will be chosen linear continuous and ψ_k constant discontinuous. This is in accordance with the necessary function spaces for the integral equations, which are not discussed here (see [33]).

Using the spatial shape functions in the boundary integral equations of the previous section results in semi-discrete equations. They can be solved either with a Galerkin or a collocation approach. Here, both techniques are presented to show their respective behavior. In particular, the Neumann problem is solved with a Galerkin method since in this case it is superior with respect to the convergence behavior compared to the collocation method.

Hence, inserting the spatial shape functions from above in the boundary integral equations (11) and applying the collocation method with the collocation points \mathbf{x}_i at the nodes results in the semi-discrete equation system

$$\mathbb{V} * \mathbf{q}^h = \mathbb{C} \mathbf{g}_D + \mathbb{K} * \mathbf{g}_D \quad \text{with} \quad \mathbb{V}[i,j] = \int_{\text{supp } \psi_j} \gamma_0 U(\mathbf{x}_i - \mathbf{y}, t - \tau) \psi_j(\mathbf{y}) \, d s_{\mathbf{y}} \quad \mathbb{K}[i,j] = \int_{\text{supp } \varphi_j} \gamma_{1,y} U(\mathbf{x}_i - \mathbf{y}, t - \tau) \varphi_j(\mathbf{y}) \, d s_{\mathbf{y}} \quad (19)$$

for the Dirichlet problem. The alternative solution is obtained by inserting the ansatz in (13) and applying the Galerkin scheme

$$\mathbf{V} * \vartheta^h = \mathbf{g}_D \quad \text{with} \quad \mathbf{V}[i, j] = \int_{\text{supp } \psi_i} \psi_i(\mathbf{x}) \int_{\text{supp } \psi_j} \gamma_0 U(\mathbf{x} - \mathbf{y}, t - \tau) \psi_j(\mathbf{y}) \, d s_{\mathbf{y}} \, d s_{\mathbf{x}} \quad (20)$$

The Neumann problem is solved by (14) using these shape functions and the Galerkin method resulting in

$$\begin{aligned} \mathbf{D} * \mathbf{u}^h &= -\frac{1}{2} \mathbf{g}_N + \mathbf{K}' * \mathbf{g}_N \quad \text{with} \\ \mathbf{D}[i, j] &= \int_{\text{supp } \varphi_i} \varphi_i(\mathbf{x}) \gamma_{1,x} \int_{\text{supp } \varphi_j} \gamma_{1,y} U(\mathbf{x} - \mathbf{y}, t - \tau) \varphi_j(\mathbf{y}) \, d s_{\mathbf{y}} \, d s_{\mathbf{x}} \\ \mathbf{K}'[i, j] &= \int_{\text{supp } \varphi_i} \varphi_i(\mathbf{x}) \gamma_{1,x} \int_{\text{supp } \varphi_j} U(\mathbf{x} - \mathbf{y}, t - \tau) \varphi_j(\mathbf{y}) \, d s_{\mathbf{y}} \, d s_{\mathbf{x}}. \end{aligned} \quad (21)$$

The given boundary data are approximated by the same shape functions, respectively. The notation with sans serif fonts or upright greek fonts in (19), (20), and (21) indicates that in these vectors the nodal values are collected.

In the Galerkin formulations double integrations have to be performed, whereas in the collocation schema only one spatial integration is necessary. The weak singular integrals in the Galerkin formulations are treated with the formula by Erichson and Sauter [16] and in the collocation scheme with a Duffy transformation [14]. The regular integrals are treated with a standard Gaussian quadrature using a heuristic distance-based formula to determine the number of Gauss points. No further treatment of quasi-singular integrals is considered.

Temporal discretisation The above given semi-discrete integral equations are discretised in time using gCQ [20, 22]. Here, the variant using Runge-Kutta methods as the underlying time stepping technique is applied. Details and the analysis can be found in [22], where here only the idea is briefly sketched using the integral equation (20).

To present the idea of the gCQ, the convolution integral in (20) is used. However, only one element of the spatial matrix vector product is shown to simplify notation. This convolution integral is reformulated using the definition of the inverse Laplace transform

$$(\mathbf{V}[i, j] * \vartheta^h[j])(t) = \int_0^t \mathbf{V}[i, j](t - \tau) \vartheta^h[j](\tau) \, d \tau = \frac{1}{2\pi i} \int_C \hat{\mathbf{V}}[i, j](s) \int_0^t e^{s(t-\tau)} \vartheta^h[j](\tau) \, d \tau \, d s, \quad (22)$$

where for the Laplace variable holds $s \in \mathbb{C}, \text{Re } s > 0$. The symbol $\hat{(\cdot)}$ denotes the Laplace transform of a function, e.g., $\hat{\mathbf{V}}[i, j](s)$ means that in (20) the fundamental solution $U(\mathbf{x} - \mathbf{y}, t - \tau)$ is replaced by $\hat{U}(\mathbf{x} - \mathbf{y}, s)$. Furthermore, the imaginary unit is denoted by $i = \sqrt{-1}$. The integration contour C is a vertical line $a - i\infty \rightarrow a + i\infty$, where a is larger than the real part of all singularities of the integral kernel. The rearrangement in (22) is valid only if the Laplace transform of the kernel function and its inverse exist. This holds true for the fundamental solutions above, where the Laplace transform of $U(\mathbf{x} - \mathbf{y}, t)$ is $\hat{U}(\mathbf{x} - \mathbf{y}, s) = \frac{1}{4\pi \|\mathbf{x} - \mathbf{y}\|} e^{-s \frac{\|\mathbf{x} - \mathbf{y}\|}{c}}$. The inner time integral is the solution of the differential equation of first order

$$\frac{\partial}{\partial t} x(t, s) = s x(t, s) + \vartheta^h[j](t) \quad \text{with} \quad x(t = 0, s) = 0. \quad (23)$$

Thus, vanishing initial conditions are required. This ordinary differential equation can be solved numerically by a time stepping method. Time is discretised in N not necessarily constant time steps Δt_i , i.e.,

$$[0, T] = [0, t_1, t_2, \dots, t_N], \quad \Delta t_i = t_i - t_{i-1}, \quad i = 1, 2, \dots, N.$$

Suppose an A- and L-stable Runge-Kutta method is given by its Butcher tableau $\begin{array}{c|c} c & A \\ \hline & b^T \end{array}$ with $A \in \mathbb{R}^{m \times m}$, $b, c \in \mathbb{R}^m$ and m is the number of stages. With the vector $\mathbb{1} = (1, 1, \dots, 1)^T$ of size m the stability function is

$$R(z) := 1 + zb^T(1 - zA)^{-1}\mathbb{1} \quad (24)$$

and A- and L-stability requires

$$|R(z)| \leq 1 \quad \text{and} \quad (1 - zA) \quad \text{is non-singular for } \Re z \leq 0 \quad \text{and} \quad \lim_{\Re z \rightarrow -\infty} R(z) = 0 \quad (25)$$

These conditions required that $b^T A^{-1} = (0, 0, \dots, 1)$ holds and they imply $c_m = 1$. These severe restrictions on the used time stepping method are based partly on the proofs, but mostly on experience [34]. With these definitions the discrete solution of the ODE (23) is [22]

$$x_n(s) = (1 - \Delta t_n s A)^{-1} \left((b^T A^{-1} x_{n-1}(s)) \mathbb{1} + \Delta t_n A (\vartheta^h[j])_n \right). \quad (26)$$

Note that the solution $x_n(s)$ is a vector containing m results at the stages for the time step n . The notation $(\cdot)_n$ indicates the discrete values of the respective function/vector or of a product at all stages corresponding to time t_n . Replacing in (22) the inner integral on the right hand side by its discrete approximation at all stages m gives

$$\begin{aligned} (V[i, j] * \vartheta^h[j])_n &= \frac{1}{2\pi i} \int_C \hat{V}[i, j](s) (1 - \Delta t_n s A)^{-1} \left(\Delta t_n A (\vartheta^h[j])_n + (b^T A^{-1} x_{n-1}(s)) \mathbb{1} \right) ds \\ &= \hat{V}[i, j] \left((\Delta t_n A)^{-1} \right) (\vartheta^h[j])_n + \frac{1}{2\pi i} \int_C \hat{V}[i, j](s) (1 - \Delta t_n s A)^{-1} (b^T A^{-1} x_{n-1}(s)) \mathbb{1} ds. \end{aligned} \quad (27)$$

Note, the notation $(V[i, j] * \vartheta^h[j])_n$ indicates a vector of size m . The first part on the right-hand side is obtained by the residue theorem, while the second term will be approximated by a quadrature rule using N_Q integration points and integration weights ω_ℓ . The parameters and integration weights used for the quadrature rule are given in A. Approximating the convolution in (20) as above gives the formula

$$(\mathbf{g}_D[i])_n = \hat{V}[i, j] \left((\Delta t_n A)^{-1} \right) (\vartheta^h[j])_n + \sum_{\ell=1}^{N_Q} \omega_\ell \hat{V}[i, j](s_\ell) (b^T A^{-1} \cdot x_{n-1}(s_\ell)) (1 - \Delta t_n s_\ell A)^{-1} \mathbb{1}. \quad (28)$$

The notation $\hat{V}[i, j] \left((\Delta t_n A)^{-1} \right)$ means that the discrete operator is not evaluated at a single complex frequency as in $\hat{V}[i, j](s_\ell)$ but at all values of the matrix entries of $(\Delta t_n A)^{-1}$. This matrix entry is therefore a matrix of size $m \times m$. Note, $(\vartheta^h[j])_n$ and $(\mathbf{g}_D[i])_n$ are also vectors of size m .

Eq (28) shows the computation of one entry in (20) at all stages m , which is the contribution of one node. Collecting these entries of all nodes in matrices $\hat{V}(\cdot)$ and analogous defined vectors $\mathbf{g}_D(t_n)$ and $(\vartheta^h)_n$, the algorithm can be given in a compact form. Note, the symbol $\hat{(\cdot)}$ has still the meaning that the Laplace transform is applied on each entry and if the argument is the matrix $(\Delta t_n A)^{-1}$ it means that in each entry we get a matrix of size $m \times m$. Considering this notation the whole algorithm can be given as in [21]

- First step

$$(\mathbf{g}_D)_1 = \hat{V} \left((\Delta t_1 A)^{-1} \right) (\vartheta^h)_1$$

with implicit assumption of zero initial condition.

- For all steps $n = 2, \dots, N$ the algorithm has two sub-steps

1. Update the solution vector \mathbf{x}_{n-1} at all integration points s_ℓ

$$\mathbf{x}_{n-1}(s_\ell) = (\mathbf{I} - \Delta t_{n-1} s_\ell \mathbf{A})^{-1} \left((\mathbf{b}^\top \mathbf{A}^{-1} \cdot \mathbf{x}_{n-2}(s_\ell)) \mathbb{1} + \Delta t_{n-1} \mathbf{A} (\vartheta^h)_{n-1} \right) \quad (29)$$

for $\ell = 1, \dots, N_Q$ with the number of integration points N_Q .

2. Compute $(\vartheta^h)_n$ solving the following linear system

$$(\mathbf{g}_D)_n = \hat{\mathbf{V}} \left((\Delta t_n \mathbf{A})^{-1} \right) (\vartheta^h)_n + \sum_{\ell=1}^{N_Q} \hat{\mathbf{V}}(s_\ell) \mathbf{W}_\ell^{\Delta t_n} ((\vartheta^h)_{n-1}) . \quad (30)$$

The abbreviation $\mathbf{W}_\ell^{\Delta t_n}((\vartheta^h)_{n-1})$ denotes a vector of size $M_2 m$, which is dependent on $\mathbf{x}_{n-1}(s_\ell)$. It collects the entries $\omega_\ell (\mathbf{b}^\top \mathbf{A}^{-1} \cdot \mathbf{x}_{n-1}(s_\ell)) (\mathbf{I} - \Delta t_n s_\ell \mathbf{A})^{-1} \mathbb{1}$ in the sum in (28) related to each node.

Essentially, this algorithm requires the evaluation of the integral kernel at N_Q points s_ℓ , which are complex frequencies. Consequently, we get an array of system matrices of size $M_2 \times M_2 \times N_Q$ beside the matrix $\hat{\mathbf{V}} \left((\Delta t_n \mathbf{A})^{-1} \right)$. This array of system matrices can be interpreted as a three-dimensional array of data which will be approximated by a data-sparse representation based on 3D-ACA.

Before describing this algorithm, the discrete set of integral equations is given. For the Dirichlet problem, we have the direct approach

$$\hat{\mathbf{V}} \left((\Delta t_n \mathbf{A})^{-1} \right) (\mathbf{q}^h)_n = \left(\mathbf{C} + \hat{\mathbf{K}} \left((\Delta t_n \mathbf{A})^{-1} \right) \right) (\mathbf{g}_D)_n + \sum_{\ell=1}^{N_Q} \left(\hat{\mathbf{K}}(s_\ell) \mathbf{W}_\ell^{\Delta t_n} ((\mathbf{g}_D)_{n-1}) - \hat{\mathbf{V}}(s_\ell) \mathbf{W}_\ell^{\Delta t_n} ((\mathbf{q}^h)_{n-1}) \right) \quad (31)$$

and the indirect approach

$$\hat{\mathbf{V}} \left((\Delta t_n \mathbf{A})^{-1} \right) (\vartheta^h)_n = (\mathbf{g}_D)_n - \sum_{\ell=1}^{N_Q} \hat{\mathbf{V}}(s_\ell) \mathbf{W}_\ell^{\Delta t_n} ((\vartheta^h)_{n-1}) . \quad (32)$$

The Neuman problem is solved with the discrete equations

$$\begin{aligned} \hat{\mathbf{D}} \left((\Delta t_n \mathbf{A})^{-1} \right) (\mathbf{u}^h)_n = \\ - \left(\frac{1}{2} \mathbf{I} - \hat{\mathbf{K}}' \left((\Delta t_n \mathbf{A})^{-1} \right) \right) (\mathbf{g}_N)_n + \sum_{\ell=1}^{N_Q} \left(\hat{\mathbf{K}}'(s_\ell) \mathbf{W}_\ell^{\Delta t_n} ((\mathbf{g}_N)_{n-1}) - \hat{\mathbf{D}}(s_\ell) \mathbf{W}_\ell^{\Delta t_n} ((\mathbf{u}^h)_{n-1}) \right) . \end{aligned} \quad (33)$$

By examining these equations the computational cost can be estimated. The computation of the matrices is $\mathcal{O}((N_Q + 1)M^2)$ and the evaluation of the time stepping method is $\mathcal{O}(N_Q N)$ matrix-vector multiplications. Note, as given in A for Runge-Kutta methods with stages $m > 1$ a suitable choice is $N_Q = N(\log(N))^2$. The solution of the equation systems in (31), (32), or (33) contributes with $\mathcal{O}(M^2 n_{iter})$. An iterative solver is necessary as long as the matrix of the actual time step is approximated with FMM or \mathcal{H} -technique. In these estimates the spatial dimension is denoted by M which is either M_2 or M_1 , respectively. The value n_{iter} is the number of iterations for the equation solver, which is usually small.

4 Three-dimensional adaptive cross approximation

An approximation of a three-dimensional array of data or a tensor of third order $\mathcal{C} \in \mathbb{C}^{M \times M \times N_Q}$ in terms of a low-rank approximation has been proposed in [9] and is referred to as a generalisation of adaptive cross approximation or also called 3D-ACA. In this approach, the 3D array of data to be approximated is generated by defining the outer product by

$$\mathcal{C} = \mathbf{H} \otimes \mathbf{f} \quad (34)$$

with $\mathbf{H} \in \mathbb{C}^{M \times M}$, $\mathbf{f} \in \mathbb{C}^{N_Q}$. The matrix \mathbf{H} corresponds to the spatial discretization of the different potentials used in the boundary element formulations from above at a specific frequency s_ℓ , e.g., the single layer potential in (32) on the right hand side. This matrix will be called face or slice and may be computed as a dense matrix or with a suitable hierarchical partition of the mesh as \mathcal{H} -matrix. Within this matrix different low-rank approximations can be applied. Here, the ACA [8] is used. Connected to this choice an hierarchical structure of the matrix has to be build with balanced cluster trees [6]. The vector \mathbf{f} , called fiber in the following, collects selected elements of \mathbf{H} at the set of frequencies determined by the gCQ. The latter would amount in N_Q entries and the same amount of faces. The 3D-ACA on the one hand approximates, as above mentioned, the faces with low rank matrices and, more importantly, the amount of necessary frequencies is adaptively determined. Hence, a sum of outer products \mathcal{C}^ℓ as given in (34) is established. The summation is stopped if \mathcal{C}^ℓ is comparable to \mathcal{C} up to a prescribed precision ε . This is measured with a Frobenius-norm. The basic concept of this approach is sketched in Algorithm 1. Essentially, three-dimensional crosses are established. These crosses consist of a face \mathbf{H}_ℓ , which is the

Algorithm 1 Pseudo code of 3D-ACA (taken from [39])

```

function 3D ACA(ENTRY,  $\varepsilon$ )  $\triangleright$  ENTRY provides the integrated kernel values at collocation point
 $x_i$  and element  $j$ 
 $\mathcal{C}^{(0)} = 0, k_1 = 0$  and  $\ell = 0$ 
while  $\|\mathbf{H}_\ell\|_F \|\mathbf{f}_\ell\|_2 > \varepsilon \|\mathcal{C}^{(\ell)}\|_F$  do
     $\ell = \ell + 1$ 
     $H_\ell[i, j] = \text{ENTRY}(i, j, k_\ell) - \mathcal{C}^{(\ell-1)}[i, j, k_\ell], \quad i, j = 1, \dots, M$ 
     $H_\ell[i_\ell, j_\ell] = \max_{i, j} |H_\ell[i, j]|$ 
     $f_\ell[k] = H_\ell[i_\ell, j_\ell]^{-1} (\text{ENTRY}(i_\ell, j_\ell, k) - \mathcal{C}^{(\ell-1)}[i_\ell, j_\ell, k]), \quad k = 1, \dots, N_Q$ 
     $\mathcal{C}^{(\ell)} = \mathcal{C}^{(\ell-1)} + \mathbf{H}_\ell \otimes \mathbf{f}_\ell$ 
     $k_{\ell+1} = \arg \max_k |f_\ell[k]|$ 
end while
 $r = \ell - 1 \quad \triangleright$  Final rank, i.e., necessary frequencies
return  $\mathcal{C}^r = \sum_{\ell=1}^r \mathbf{H}_\ell \otimes \mathbf{f}_\ell$ 
end function

```

respective matrix at a distinct frequency s_ℓ times a fiber \mathbf{f}_ℓ , which contains one matrix entry, the pivot element, at all N_Q frequencies. These crosses are added up until a predefined error is obtained. The amount of used frequencies is the so-called rank r of this approximation of the initial data cube. The mentioned pivot element is denoted in Algorithm 1 with $H_\ell[i_\ell, j_\ell]$. Like in the 'normal' ACA this pivot element can be selected arbitrarily. However, selecting the maximum element ensures convergence. For details see [9] or the application using \mathcal{H}^2 -matrices in the faces [39].

The stopping criterion requires a norm evaluation of $\mathcal{C}^{(\ell)}$. Assuming some monotonicity the norm can be computed recursively

$$\left\| \mathcal{C}^{(\ell)} \right\|_F^2 = \sum_{d, d'}^{\ell} \left(\sum_{i, j} H_d[i, j] \overline{H_{d'}[i, j]} \right) \left(\sum_k f_d[k] \overline{f_{d'}[k]} \right) \quad (35)$$

following [39].

The multiplication of the three-dimensional data array with a vector is changed by the proposed algorithm. Essentially, the algorithm separates the frequency dependency such that $\mathbf{H}_\ell(\hat{\mathbf{V}})$ is independent of the frequency and the fibers $\mathbf{f}_\ell(\hat{\mathbf{V}})$ present this dependency. Let us use the multiplication on the right hand side of (32) as example. The multiplication is changed to

$$\sum_{\ell=1}^{N_Q} \hat{\mathbf{V}}(s_\ell) \mathbf{W}_\ell^{\Delta n} = \sum_{\ell=1}^{N_Q} \sum_{k=1}^r \mathbf{H}_k(\hat{\mathbf{V}}) \otimes f_k[\ell](\hat{\mathbf{V}}) \mathbf{W}_\ell^{\Delta n} = \sum_{k=1}^r \mathbf{H}_k(\hat{\mathbf{V}}) \otimes \sum_{\ell=1}^{N_Q} f_k[\ell](\hat{\mathbf{V}}) \mathbf{W}_\ell^{\Delta n}. \quad (36)$$

The complexity of the original operation is $\mathcal{O}(N_Q M^2)$ for M spatial unknowns. The approximated version has the complexity $\mathcal{O}(r(M^2 + N_Q))$. It consists of the inner sum, which requires N_Q multiplications, and the outer sum which is a matrix times vector multiplication of size M . Hence, the leading term with M^2 has only a factor of r instead of N_Q compared to the dense computation. It can be expected that for larger problem sizes with a significant reduction from N_Q to r complex frequencies this discrete convolution is faster.

Remarks for the implementation:

- There are two possibilities how to apply the 3D-ACA within the above given boundary element formulations. Either it can be applied on each matrix block, which requires that for the different frequencies the same hierarchical structure is used. This holds here as a pure geometrical admissibility criterium for the \mathcal{H} -matrix has been selected. The other choice would be to apply 3D-ACA on the \mathcal{H} -matrix as a whole. In the latter case the stopping criterion is determined by all matrix blocks, i.e., (35) is evaluated for each block and summed up. Consequently, the matrix block with the largest rank determines the overall rank. Hence, this choice results in a less efficient formulation as shown in [37]. Nevertheless, if the matrix structure in the different \mathbf{H}_ℓ differ this choice is a solution.
- In each face the ACA is used to compress these matrices beside the rank reduction with respect to the frequencies. Here, a recompression of the ACA is applied, which gives a representation of the admissible matrix blocks in a SVD like form $\mathcal{A} \approx \mathcal{A}_r = \mathbf{U}\Sigma\mathbf{V}^H$. Starting from the low rank representation of a block $\mathcal{A}_r = \mathbf{U}\mathbf{V}$, a QR-decomposition of the low-rank matrix \mathbf{U} and \mathbf{V} is performed

$$\mathcal{A} \approx \mathcal{A}_r = \mathbf{U}\mathbf{V}^H = \mathbf{Q}_U(\mathbf{R}_U\mathbf{R}_V^H)\mathbf{Q}_V^H = \mathbf{Q}_U\check{\mathbf{U}}\check{\Sigma}\check{\mathbf{V}}^H\mathbf{Q}_V^H = \check{\mathbf{U}}\check{\Sigma}\check{\mathbf{V}}^H \quad (37)$$

and, secondly, the SVD is applied on the smaller inner matrix $\mathbf{R}_U\mathbf{R}_V^H$. The sketched technique improves the compression rates.

- Within the algorithm the largest element in a matrix block has to be found. For non-admissible blocks this operation requires to compare all block entries. For admissible blocks the elements are not available directly and, hence, has either be computed out of the low-rank representation or an estimate can be used. Due to the recompression of the ACA-blocks low-rank matrices $\check{\mathbf{U}}$ and $\check{\mathbf{V}}$ consist of orthonormal columns and the estimation of the index i of the pivot position can be found with

$$\arg \max_{i,j} |a_{ij}| = \arg \max_{i,j} \sum_{k=1}^r |u_{ik}\sigma_k| \underbrace{|v_{jk}|}_{\leq 1} \leq \arg \max_i \sum_{k=1}^r |u_{ik}\sigma_k|. \quad (38)$$

The analogous way is used also for index j . This algorithm gives a pivot element which is approximately the largest element. However, in the computation of the fiber the original entries are used. Hence, the computation of the residuum is an approximation. For the single layer potential this approximation works fine but not for the double layer potential. In this case, the maximal element is determined by multiplying the low rank matrices, finding the largest element and deleting this dense block. Fortunately, such matrix operations can be efficiently implemented such that the computing time is not affected. Hence, in the presented results for all potentials this expanding to the dense matrix block is used.

5 Numerical examples

The above proposed method to accelerate the gCQ based time domain boundary element method is tested at three examples. First, a unit cube is used, second a cube with a reentrant corner (three-dimensional L-Shape), and third a unit ball. The first two test geometries are used for Dirichlet and Neumann problems, whereas in case of the unit ball only a Dirichlet problem is studied. For the latter case a non-smooth timely response of the solution has to be tackled. In all tests the main goal is to show that the approximation of the 3D-ACA does not spoil the results, i.e., the newly introduced approximation error is smaller than the error of the dense BE formulation. Main focus is on the overall obtained reduction in storage, i.e., the compression which is measured as the relation between the dense storage and the storage necessary for the proposed method.

To show that the 3D-ACA does not spoil the results the error in space and time is measured with

$$\begin{aligned} L_{max}(u_h) &= \max_{1 \leq n \leq N} \left\| u \left(\frac{t_n + t_{n+1}}{2} \right) - u_h \left(\frac{t_n + t_{n+1}}{2} \right) \right\|_{L_2} \\ &= \max_{1 \leq n \leq N} \sqrt{\int_{\Gamma} \left(u \left(\mathbf{x}, \frac{t_n + t_{n-1}}{2} \right) - u_h \left(\mathbf{x}, \frac{t_n + t_{n-1}}{2} \right) \right)^2 d\Gamma}, \end{aligned} \quad (39)$$

where u and u_h are placeholders for the presented quantity measured at the boundary of the selected domain Γ . The same error has been used in [32]. It computes the usual L_2 -error with respect to the spatial variable and takes the largest value of them in all time steps. The convergence rate is denoted by

$$eoc = \log_2 \left(\frac{L_{max}^h}{L_{max}^{h+1}} \right), \quad (40)$$

where the superscript h and $h + 1$ denotes two subsequent refinement level. The convergence results presented below does not change significantly if an L_2 -error in time would be used as long as the time response is smooth. For the results of the sphere in the third subsection the drop in convergence is not that significant for an L_2 -error in time as such a measure smears the error in time over all time steps.

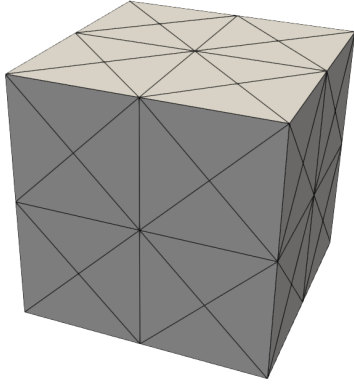
As mentioned above, linear triangles are used for the discretisation of the geometry and either linear continuous or constant discontinuous shape functions for the unknown Cauchy data in the direct method are applied. In the indirect method constant discontinuous shape functions for the density are selected. The underlying time stepping method has been the 2-stage Radau IIA. The approximation within the faces has been chosen to be $\varepsilon_{ACA} = 10^{-4} \dots 10^{-8}$ for the different refinement levels of the spatial discretisation. In each refinement level the mesh size is halved as well as the time step size. The ratio of time steps to mesh size was kept constant with 0.7. The precision of the method with respect to the frequencies, i.e., the ε in Algorithm 1 was selected as $\varepsilon = 100 * \varepsilon_{ACA}$. The final equation is solved with BiCGstab without any preconditioner, where the precision ε_{ACA} is set. All results are computed for a wave speed $c = 1$ m/s.

5.1 Example: Unit cube loaded by a smooth pulse

The first used test geometry is a unit cube $[-0.5, 0.5]^3$ with the coordinate system located in the middle of the cube. In Fig. 1, this cube is displayed with the mesh of refinement level 1 and the table of all used meshes is given aside. These meshes are created by bisecting the cathetus of the coarser mesh. As load a smooth pulse

$$u(\mathbf{y}, t) = \frac{\left(t - \frac{r}{c}\right)^2}{r} e^{-c\left(t - \frac{r}{c}\right)} H\left(t - \frac{r}{c}\right) \quad \text{with } r = \|\mathbf{x} - \mathbf{y}\| \quad (41)$$

at the excitation point $\mathbf{x} = (0.8, 0.2, 0.3)^\top$ is used for the Dirichlet problem. For the Neumann problem the same geometry but with inverted normals, i.e., a cavity with the shape of the cube, is used. In this



(a) Unit cube (level 1, $h = 0.5$ m)

level	nodes	elements	h	Δt
1	50	96	0.5 m	0.3 s
2	194	384	0.25 m	0.15 s
3	770	1536	0.125 m	0.075 s
4	3074	6144	0.0625 m	0.0375 s
5	12290	24576	0.03125 m	0.01875 s

(b) Used meshes

Figure 1: Unit cube: Geometry and discretisation parameters

case the excitation point is at $\mathbf{x} = (0.3, -0.2, 0.4)^\top$. The total observation time $T = 3$ s is selected such that the smooth pulse travels over the whole unit cube.

In the following, the results are discussed for a Dirichlet problem using (31) with a collocation approach and a Neumann problem using (33) with a Galerkin approach. In Fig. 2, the L_{max} -error defined in (39) is presented versus the different refinement levels, where ‘No Lwr’ means a computation applying the 3D-ACA but for the faces instead of the ACA dense matrix blocks are applied, i.e., the approximation is only with respect to the complex frequencies. The phrase ‘dense’ means no 3D-ACA at all and ‘ACA’

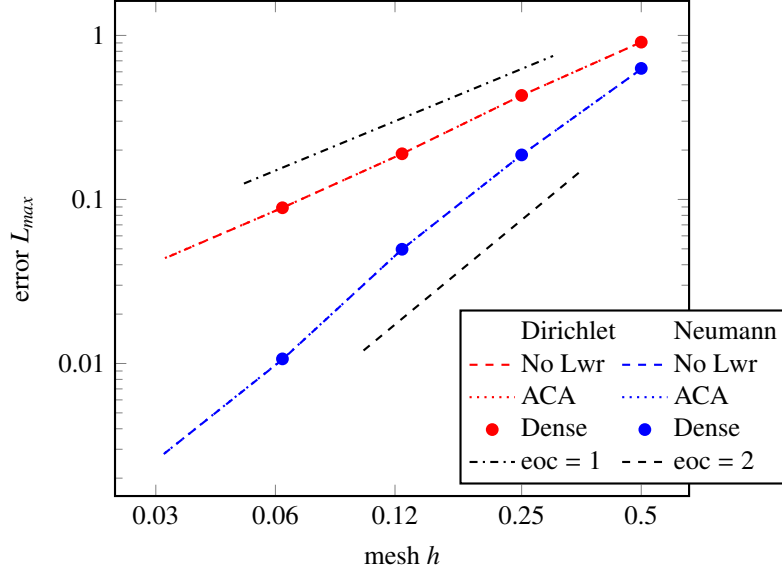


Figure 2: Cube: L_{max} -error versus refinement in space and time

states that the algorithm from above is used with an ACA approximation also in the faces. Note, the refinement is done in space and time, i.e., not only h is changed but as well Δt . The numbers displayed at this axis refer to the element size h . The expected order of convergence is obtained considering that two factors influence the error. First, the spatial discretisation is expected to yield for a refinement in space a linear order for the constant shape functions used for the single layer potential, whereas the linear shape functions would result in a quadratic order for the hypersingular operator. These spatial known errors for the respective elliptic problem are combined with the 2-stage Radau IIA method used within the gCQ.

This method would allow a third order convergence. However, as the spatial convergence orders are smaller they will dominate. This is clearly observed in Fig. 2. The second observation is that the 3D-ACA does not spoil the results. Certainly, the ε -parameters have to be adjusted carefully. As mentioned above, the ACA in the faces starts with $\varepsilon_{ACA} = 10^{-4}$ in the coarsest level and is increased by 10^{-1} in each level up to $\varepsilon_{ACA} = 10^{-8}$. The gCQ Algorithm 1 is terminated with $\varepsilon = 100 * \varepsilon_{ACA}$. Both parameters are found by trial and error.

After this check of a correct implementation and showing that the compression does not spoil the results, the efficiency with respect to the used frequencies, i.e., the rank in the third matrix dimension is studied. This gain of the 3D-ACA is presented in the Figs. 3 and 4 for the Dirichlet and Neumann problem, respectively. In both figures, the amount of used complex frequencies is given with respect to the mesh size, i.e., the refinement level. Due to the selection of the different problems all of the four layer

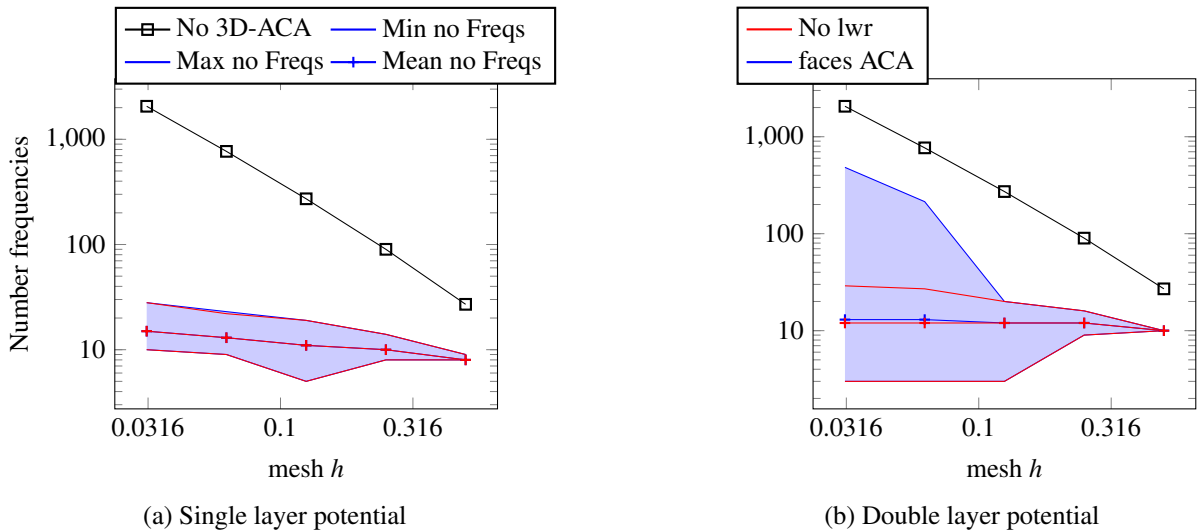


Figure 3: Cube: Number of used frequencies for the Dirichlet problem

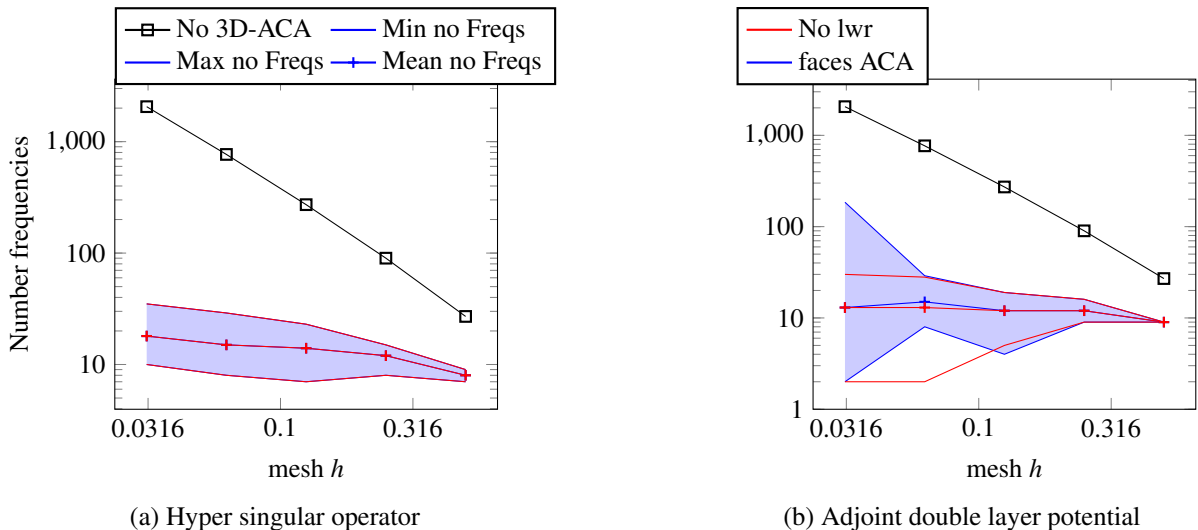


Figure 4: Cube: Number of used frequencies for the Neumann problem

potentials from above are studied. Note, as the 3D-ACA is applied on the matrix blocks of the \mathcal{H} -matrix, each matrix block may have its own number of necessary complex frequencies. That is why a min-, max- and mean-value is given. Further, the numbers are displayed for the version using no approximation in the faces (red) and those with an ACA approximation within the faces (blue). Essentially, all operators

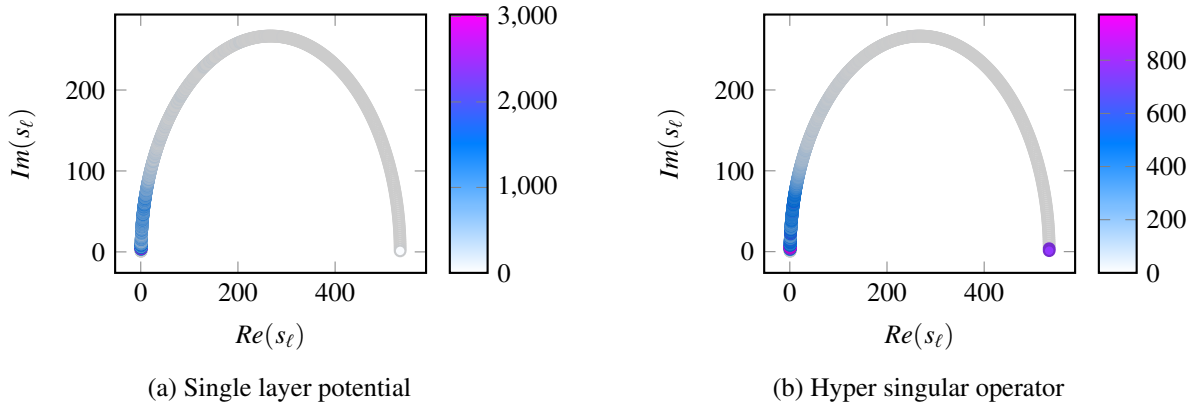


Figure 5: Cube (level 4): Used complex frequencies with a colour code for the number of matrix blocks, where this frequency is active

show a drastic reduce of the used frequencies resulting in a drastic reduction of memory usage. Further, for more time steps (reducing time step size) only a very moderate increase in the number of frequencies is visible. Only for the double layer potentials the approximation with ACA significantly changes the maximum number of used frequencies, however not in the mean value. This is caused by the structure of the double layer potential, which includes on the one hand changing normal vectors resulting in blocks, which are badly approximated by ACA, and zero blocks. The zero blocks are not considered, however some frequencies are tested to make sure that the block under consideration is indeed a zero block. This results in the very low number of the min-value. The higher max values result from difficulties to determine the norm with (35) as the monotonicity is not that good in the above discussed blocks.

To display the adaptively selected frequencies, in Fig. 5 the complex frequencies of the gCQ are plotted in the complex plane exemplarily for level 4. A dense formulation would use all frequencies. The colour code shows how much blocks in the 3D-ACA are evaluated at these frequencies. As the algorithm starts for all blocks with the first frequency selected by gCQ, this frequency is selected by all blocks (22432 for the single layer potential and 8560 for the hyper singular operator). This number is deleted from the plot because else nothing would be visible due to the linear scaled colour range. The figure clearly shows that there is a region with small real parts where significant frequencies are detected by the algorithm. Surprisingly, the last complex frequency with large real part and nearly vanishing imaginary part is as well selected in case of the hypersingular operator. The same happens for the single layer potential, however for much less frequencies such that it is not visible in the plots above. For both double layer potentials similar pictures could be shown, where also for the adjoint double layer potential the last frequency is more often selected.

The above results indicate that the memory requirement of the proposed method is strongly improved compared to the standard formulation. As the right hand side is multiplied on the fly, i.e., the storage is the same for the new and the original formulation, the compression is only determined by the single layer and hypersingular operator in the Dirichlet and Neumann problem, respectively. This compression is plotted in Fig. 6 for both problems, Dirichlet and Neumann, versus the refinement. As mentioned above, the compression is the relation between the required storage for the proposed formulation divided by the storage of a dense formulation. Obviously, the improvement is very strong, where the difference between the version without a compression in the face to the results with the ACA applied in the faces is not that strong. This is understandable if the sizes of the faces are considered. Those are not that large such that ACA can achieve a substantial improvement. Nevertheless, a compression of up to 0,56 % is a very good result.

Concerning the computing time a not that clear picture is possible. The presented results have been computed on one cluster node with 64 cores and 1 TB of storage. The code uses OpenMP for the obvious parallelisation with respect to the \mathcal{H} -matrix blocks. First, the complexity of the dense algorithm is

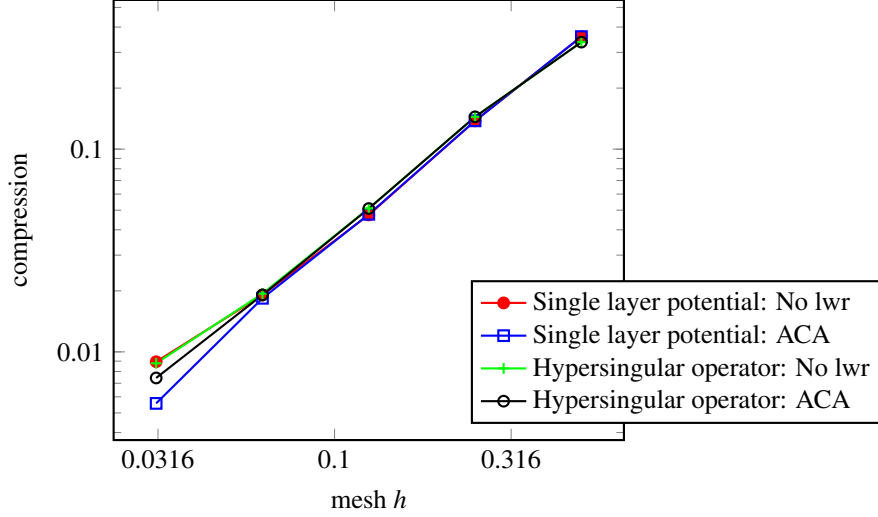


Figure 6: Cube: Compression of the data-sparse representation

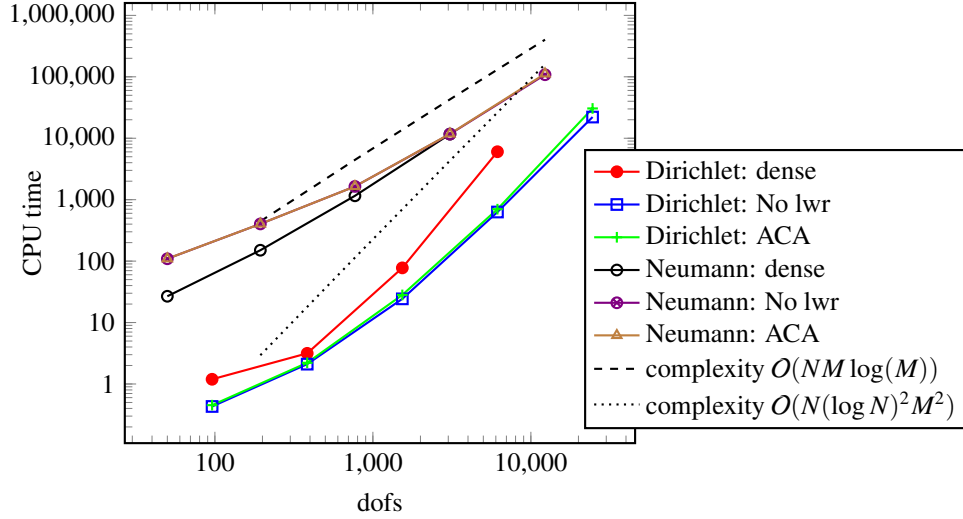
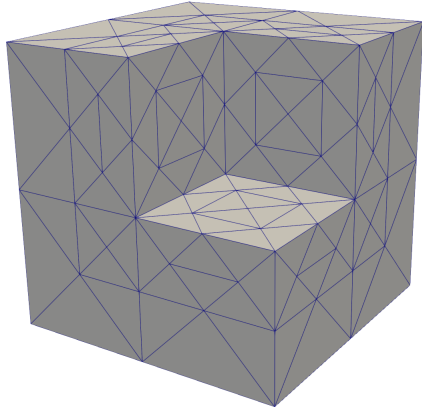


Figure 7: Cube: CPU time of the data-sparse representation

$\mathcal{O}(N(\log(N))^2 M^2)$. This line is plotted in Fig. 7 as dotted line. The dense Dirichlet problem follows this line, however, the Neumann problem not that clear. The reason might be the Galerkin formulation, which dominates the spatial matrix element calculation, and maybe avoids to be in the asymptotic range. The data sparse computations are clearly faster for the Dirichlet problem compared to the dense one but for the Neumann problem the advantage is not yet visible. Again it should be remarked that the Neumann problem uses a Galerkin method and the Dirichlet problem a collocation method. For the 3D-ACA the complexity line $\mathcal{O}(NM \log(M))$ seems to fit. However, it must be remarked that there is not any reason why this should hold. There is no indication in the algorithm that the adaptively determined rank r is linear in N . Overall, it can be concluded that the 3D-ACA gives a very good performance with respect to the storage reduction but not that much savings in the CPU-time.

5.2 Example: Unit cube with reentrant corner (L-Shape) loaded by a smooth pulse

The next example is the same study as above but with a different geometry. The selected geometry is the three-dimensional version of an L-shape, i.e., a cube with a reentrant corner. The geometry as well as the parameters of the used meshes are given in Fig. 8. The total observation time $T = 3$ s is selected



(a) L-Shape (level 1, $h = 0.5$ m)

level	nodes	elements	h	Δt
1	95	186	0.5 m	0.3 s
2	374	744	0.25 m	0.15 s
3	1490	2976	0.125 m	0.075 s
4	5954	11904	0.0625 m	0.0375 s
5	23810	47616	0.03125 m	0.01875 s

(b) Used meshes

Figure 8: L-Shape: Geometry and discretisation parameters

such that the smooth pulse travels over the whole computing domain. Note, the value h in the table in Fig. 8 is misleading as it gives values of the largest elements, which are located on the not visible sides. Those elements on the side edges of the L-Shape on the left and right side have these sizes as well. Hence, towards the reentrant corner the mesh is refined compared to h . As above, a Dirichlet and a Neumann problem is studied. For both, the excitation point is selected in the reentrant part at $\mathbf{x} = (0.25, 0.25, 0.25)^T$ and the load is the same smooth puls of (41). Note, the origin of the coordinate system is again in the center of the unit cube. Different to the setting above the Neumann problem is now not a scattering problem but computes the pressure at the surface of this L-Shape. The used equations are again (31) for the Dirichlet problem solved with a collocation approach and the Neumann problem uses (33) with a Galerkin approach.

First, as in the test above the convergence rates are reported to show that the proposed method keeps the error level of the dense computation. In Fig. 9, the L_{max} -error is plotted versus the refinement in space and time for the Dirichlet and Neumann problem. In this figure three lines are visible. The Dirichlet

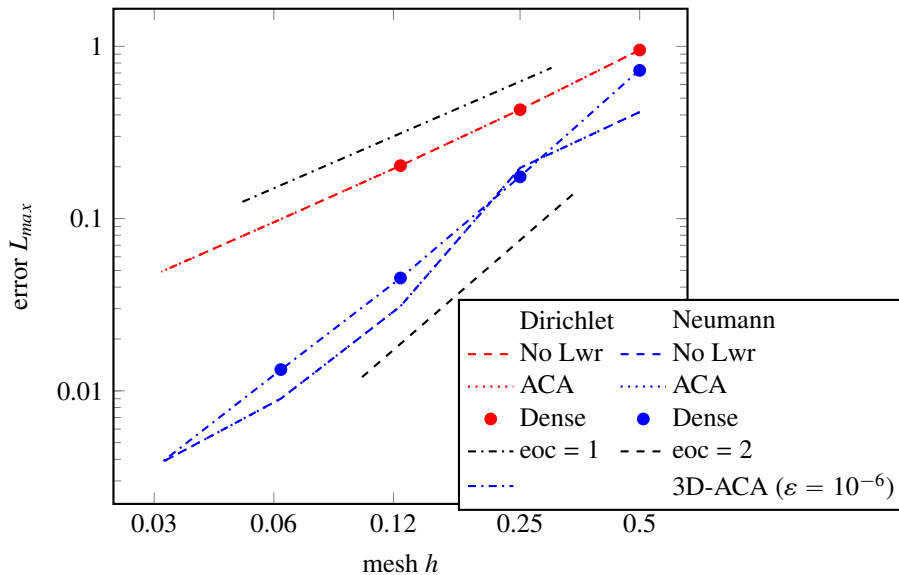


Figure 9: L-Shape: L_{max} -error versus refinement in space and time

problem is solved with the expected convergence rate and the dense computation gives the same results. For the Neumann problem the rate is still obtained also with the 3D-ACA but the error level is different.

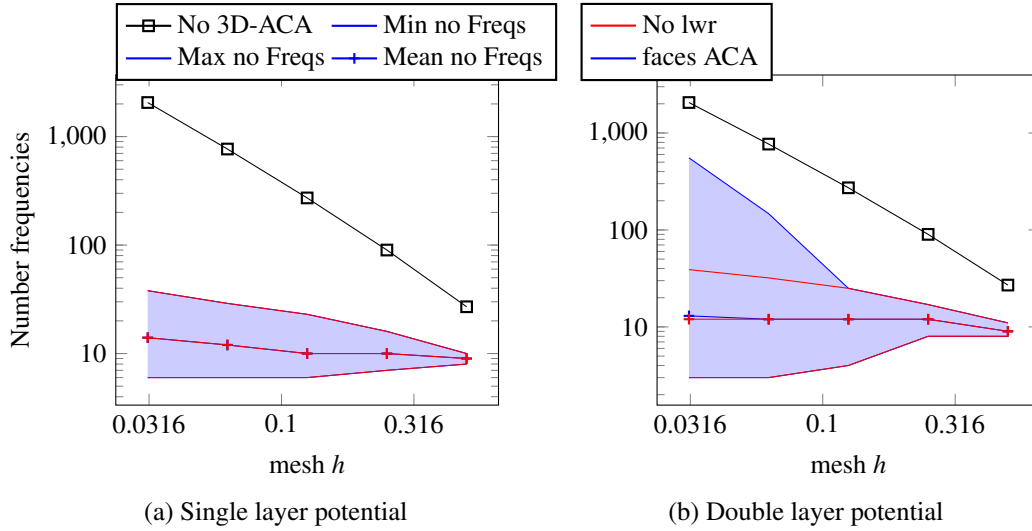


Figure 10: L-Shape: Number of used frequencies for the Dirichlet problem

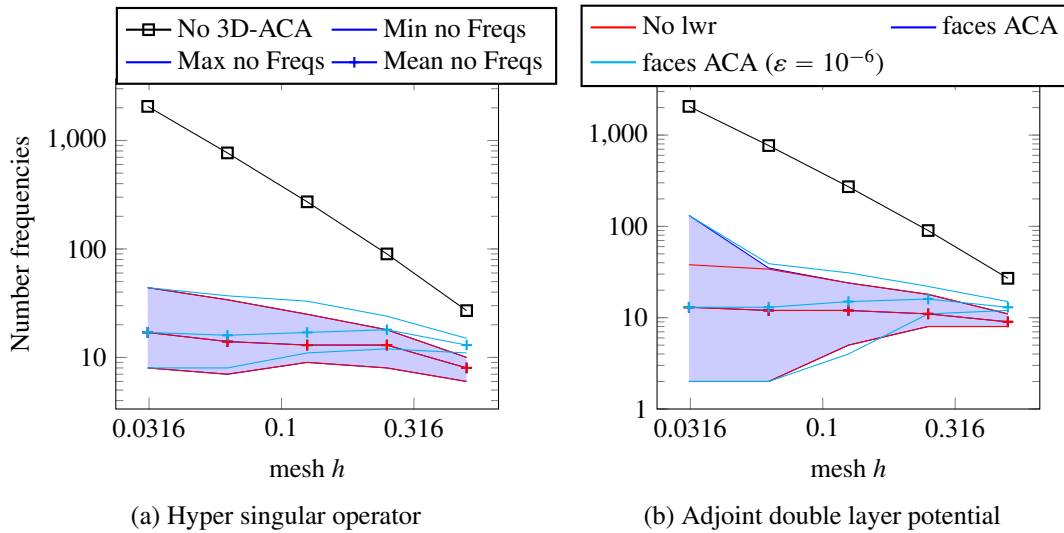


Figure 11: L-Shape: Number of used frequencies for the Neumann problem

However, as indicated with the line '3D-ACA ($\epsilon = 10^{-6}$)' it is shown that for an increased precession the dense results can be recovered. This result confirms that the 3D-ACA has an influence on the computation and the ϵ -parameter must be carefully adjusted, despite that in this case the coarser approximation gives better results.

The used complex frequencies are as well studied for this geometry. They are displayed in Figs. 10 and 11. Essentially, the pictures are similar to those for the unit cube and the numbers are comparable. Hence, there is no evidence that the geometry affects the used frequencies. Another remarkable point is the different numbers for an increased precession value ϵ . For the smaller meshes and less time steps the difference in the mean value is clearly visible but with increasing numbers for the times steps this difference vanishes. Hence, it may be concluded that the adaptivity inherently in the proposed algorithm detects the amount of frequencies necessary to give the physical behaviour of the solution. The compression rates are comparable to the unit cube and also the selection of the complex frequencies. Hence, these figures are skipped for the sake of brevity.

5.3 Example: Unit ball (sphere) loaded by a non-smooth pulse

The next example is used to show the influence of the time step size on the proposed method. The main feature of gCQ is to allow variable time step sizes to improve the approximation of solutions. Such gradings in time are necessary for non-smooth time behaviour of the solution. In the paper studying the numerical behaviour of the gCQ [21], a solution is selected where the behaviour in time is non-smooth such that a grading in the time mesh makes sense. This example is also used here to show the ability of the proposed approximation method to handle as well such solutions.

The selected geometry is a ball (sphere) with radius 1 m. The geometry and the selected mesh are shown in Fig. 12. Different to the examples above, here, the spatial discretisation is not changed. This

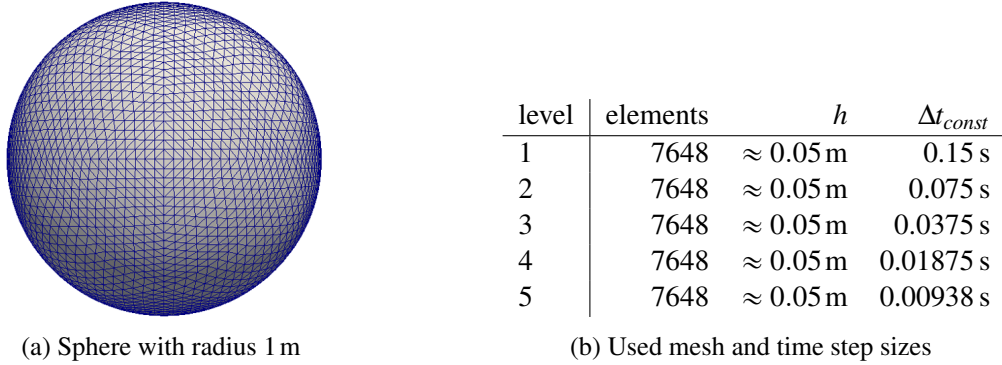


Figure 12: Sphere: Geometry, mesh size and used time step sizes

is motivated by the constructed solution. It is known that the density function within a single layer approach for the sphere corresponds to the spherical harmonics times the time derivative of the applied excitation in time [31]. Selecting the zeroth order spherical harmonic $Y_0^0(\mathbf{x})$, the spatial solution is a constant function. This part of the solution is decoupled from the temporal solution, which might justify to keep the spatial discretisation constant and refine only in time. The selected excitation and analytical solution is

$$g_D(\mathbf{x}, t) = Y_0^0(\mathbf{x}) t^{\frac{3}{2}} e^{-t} \quad \Rightarrow \quad \vartheta(\mathbf{x}, t) = Y_0^0(\mathbf{x}) \sum_{k=0}^{\lfloor t/2 \rfloor} e^{-(t-2k)} \left(\frac{3}{2} (t-2k)^{\frac{1}{2}} - (t-2k)^{\frac{3}{2}} \right). \quad (42)$$

The term with the square root shows a non-smooth behaviour in time starting at $t = 0$ s and is repeated in a periodic manner. Selecting the total observation time $T = 1.5$ s results in a solution, where the non-smooth part is only at the beginning. Hence, a graded time mesh

$$t_n = T \left(\frac{n}{N} \right)^\alpha = N \Delta t_{const} \left(\frac{n}{N} \right)^\alpha \quad n = 0, 1, \dots, N \quad (43)$$

can be recommended. The value Δt_{const} is introduced to clarify the meaning of time step size, i.e., in Fig. 12 this value is listed. For $\alpha = 2$ the full convergence order should be preserved. The effect of the grading can be observed in Fig. 13, where the L_{max} -error is presented versus a refinement in time for different exponents α . The value $\alpha = 1$ corresponds to a constant step size, where as expected the convergence order decreases to $eoc = 0.5$. With the graded mesh the convergence order is recovered. Note, the density function is approximated by constant shape functions, hence a order larger than 1 can not be expected. Obviously, there is a break in the convergence, where a further decrease of the time step size does not improve the result. This behaviour is already reported in [21] and reflects that the spatial discretisation is no longer suitable in combination with the spatial integration. Using the analytical solution in the spatial variable allows gCQ to keep the convergence order (see [21]). The proposed accelerated algorithm shows obviously the same behaviour. Hence, the approximation due to the 3D-ACA does not affect the efficiency of the gCQ based time domain BEM.

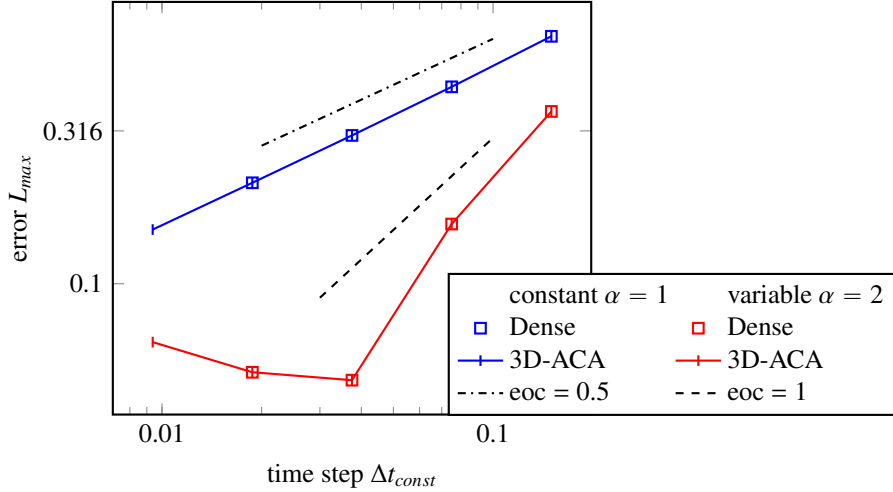


Figure 13: Sphere: L_{max} -error versus time step size for constant and variable time step size

Next, the used complex frequencies are studied for this example. In Fig. 14, the amount of used complex frequencies is plotted for both temporal discretisations. Obviously, the graded time mesh requires

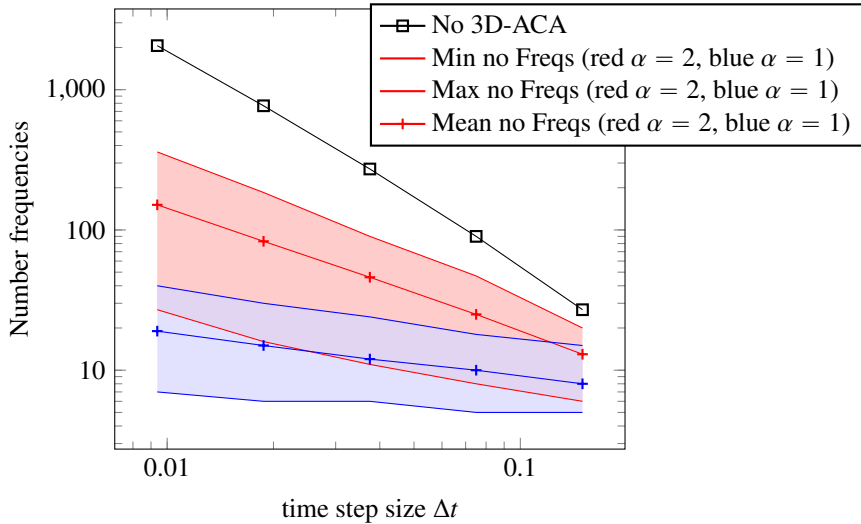


Figure 14: Sphere: Necessary frequencies for 3D-ACA where also the faces uses ACA

more frequencies compared to the constant discretisation. This holds true in the mean-value as well as in the max- and min-values. The tendency is as well that in this case the mean value does not approach a nearly constant amount of time steps. However, the increase is significantly smaller than in the dense method and very good compression can be obtained. The compression is for the first level 26% and in the fifth level 0,98 %. This reduction in storage is significant and allows to treat larger problems. Unfortunately, for $\alpha = 2$ the computation time increases compared to the uniform time step. If the same accuracy is observed, i.e., comparing the computing time of refinement level 2 for $\alpha = 2$ with level 5 for $\alpha = 1$ (see Fig. 13), almost a factor of 2 is measured (7746 sec to 4295 sec). The variable step size does not pay off in this example even when using 3D-ACA.

For this example it is interesting to report not only the numbers of used frequencies but also which frequencies are selected. In Fig. 15, the same plots as presented for the unit cube are shown. First, looking at the right plot for the graded time mesh $\alpha = 2$ it can be clearly seen how focused the frequencies are towards the imaginary axis and small real values. It is even visible that for large real values a coarsening happens. This is in accordance with the integration rule. The difference between the largest and smallest

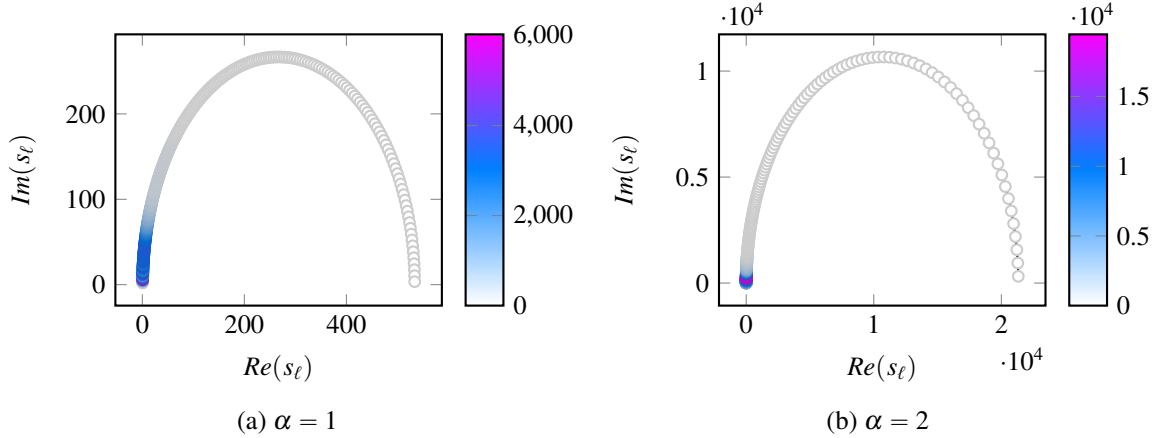


Figure 15: Sphere (level 3): Used complex frequencies with a colour code for the number of matrix blocks, where this frequency is active

time step (parameter q in A) determines the concentration of the frequencies towards the imaginary axis. Another effect independent of the 3D-ACA is the much larger values of the complex frequencies, i.e., the circle is larger. Please, have a look at the values on the axis compared to the left picture. Somehow as a consequence of this concentration as well the selected frequencies are concentrated towards small real values. It seems that the 3D-ACA preserves the properties of the integration rule.

6 Conclusions

Time domain boundary element formulations are usually very storage demanding as a lot of matrices for several time steps have to be stored. This is as well a significant drawback for the generalised convolution quadrature (gCQ) based formulation, where approximately $N \log N$ or more matrices each of the size of an elliptic problem have to be stored or more precise kept in memory. This reduces possible applications to very small sizes. The generalised adaptive cross approximation (3D-ACA) allows to find a low rank representations of three-dimensional tensors, hence this method is applied here to a gCQ based time domain BEM.

The results show a very significant reduction in storage while keeping the convergence of a dense computation. The algorithm is somehow a black-box technique as no modifications of the existing kernels of the dense formulation is necessary. The presented studies show the storage reduction for three different geometries, a unit cube, an L-shape, and a sphere. All three show similar behaviour with respect to the adaptively selected complex frequencies of the gCQ. The example with the sphere shows as well that the benefit of gCQ to select non-uniform time steps can be preserved, however for strongly different time step sizes the amount of necessary frequencies increases. Summarising, the application of 3D-ACA on the gCQ based time domain BEM gives a data sparse method with storage savings of more than 99%.

Acknowledgement The work of M. Schanz is partially supported by the joint DFG/FWF Collaborative Research Centre CREATOR (DFG: Project-ID 492661287/TRR 361; FWF: 10.55776/F90) at TU Darmstadt, TU Graz and JKU Linz.

A Parameters of the gCQ

The derivation and reasoning how the integration weights and points are determined can be found in [21, 22]. The result of these papers are recalled here. The integration points in the complex plane are

$$s_\ell = \gamma(\sigma_\ell), \quad \omega_\ell = \frac{4K(k^2)}{1\pi i} \gamma'(\sigma_\ell), \quad N_Q = N \log(N),$$

where for Runge-Kutta methods with $m > 1$ stages it should be $N_Q = N(\log(N))^2$. $K(k)$ is the complete elliptic integral of first kind

$$K(k) = \int_0^1 \frac{dx}{\sqrt{(1-x^2)(1-k^2x^2)}}, \quad K'(k) = K(1-k)$$

and K' is its derivative, which equals the integral of the complementary modulus. The argument k depends on the relation q of the maximum and minimum step sizes in the following way

$$k = \frac{q - \sqrt{2q-1}}{q + \sqrt{2q-1}} \quad q = 5 \frac{\Delta t_{\max} \max_i |\lambda_i(A)|}{\Delta t_{\min} \min_i |\lambda_i(A)|},$$

with the eigenvalues $\lambda_i(A)$. For the implicit Euler method the eigenvalues are 1 and the factor 5 in q can be skipped. The functions $\gamma(\sigma_\ell)$ and $\gamma'(\sigma_\ell)$ are

$$\begin{aligned} \gamma(\sigma_\ell) &= \frac{1}{\Delta t_{\min}(q-1)} \left(\sqrt{2q-1} \frac{k^{-1} + \text{sn}(\sigma_\ell)}{k^{-1} - \text{sn}(\sigma_\ell)} - 1 \right) \\ \gamma'(\sigma_\ell) &= \frac{\sqrt{2q-1}}{\Delta t_{\min}(q-1)} \frac{2 \text{cn}(\sigma_\ell) \text{dn}(\sigma_\ell)}{k(k^{-1} - \text{sn}(\sigma_\ell))^2} \\ \sigma_\ell &= -K(k^2) + \left(\ell - \frac{1}{2} \right) \frac{4K(k^2)}{N_Q} + \frac{i}{2} K'(k^2), \end{aligned}$$

where $\text{sn}(\sigma_\ell)$, $\text{cn}(\sigma_\ell)$ and $\text{dn}(\sigma_\ell)$ are the Jacobi elliptic functions. As seen from above, the integration contour is only determined by the largest and the smallest time steps chosen but not dependent on any intermediate step sizes. Due to the symmetric distribution of the integration points with respect to the real axis, only half of the frequencies s_ℓ need to be calculated.

Last, it may be remarked that for constant time steps $\Delta t_i = \text{const}$ the parameter determination would fail because this choice results in $q = 1$ and $k = 0$. Unfortunately, this value is not allowed for the complete elliptic integral. However, a slight change in the parameter $q \approx 1$ fixes this problem without spoiling the algorithm. The latter can be done as these parameter choices are empirical.

References

- [1] A. Aimi and M. Diligenti. A new space-time energetic formulation for wave propagation analysis in layered media by BEMs. *Int. J. Numer. Methods. Engrg.*, 75(9):1102–1132, 2008.
- [2] A. Aimi, M. Diligenti, A. Frangi, and C. Guardasoni. A stable 3d energetic Galerkin BEM approach for wave propagation interior problems. *Eng. Anal. Bound. Elem.*, 36(12):1756–1765, 2012. ISSN 0955-7997. doi: <http://dx.doi.org/10.1016/j.enganabound.2012.06.003>. URL <http://www.sciencedirect.com/science/article/pii/S0955799712001361>.
- [3] A. Bamberger and T. Ha-Duong. Formulation variationnelle espace-temps pour le calcul par potentiel retardé d'une onde acoustique. *Math. Meth. Appl. Sci.*, 8:405–435 and 598–608, 1986.

- [4] L. Banjai and M. Kachanovska. Fast convolution quadrature for the wave equation in three dimensions. *J. Comput. Phys.*, 279:103–126, 2014. ISSN 0021-9991. doi: <https://doi.org/10.1016/j.jcp.2014.08.049>. URL <https://www.sciencedirect.com/science/article/pii/S0021999114006251>.
- [5] L. Banjai and S. Sauter. Rapid solution of the wave equation in unbounded domains. *SIAM J. Numer. Anal.*, 47(1):227–249, 2008.
- [6] M. Bebendorf. *Hierarchical Matrices: A Means to Efficiently Solve Elliptic Boundary Value Problems*, volume 63 of *Lecture Notes in Computational Science and Engineering*. Springer-Verlag, 2008.
- [7] M. Bebendorf. Adaptive cross approximation of multivariate functions. *Constr. Approx.*, 34(2):149–179, 2011. doi: 10.1007/s00365-010-9103-x. URL <https://doi.org/10.1007/s00365-010-9103-x>.
- [8] M. Bebendorf and S. Rjasanow. Adaptive low-rank approximation of collocation matrices. *Computing*, 70:1–24, 2003.
- [9] M. Bebendorf, A. Kühnemund, and S. Rjasanow. An equi-directional generalization of adaptive cross approximation for higher-order tensors. *Appl. Num. Math.*, 74:1–16, 2013. ISSN 0168-9274. doi: <https://doi.org/10.1016/j.apnum.2013.08.001>. URL <http://www.sciencedirect.com/science/article/pii/S0168927413000950>.
- [10] M. Costabel. Time-dependent problems with the boundary integral equation method. In E. Stein, R. de Borst, and T. J. R. Hughes, editors, *Encyclopedia of Computational Mechanics*, volume 1, Fundamentals, chapter 25, pages 703–721. John Wiley & Sons, New York, Chichester, Weinheim, 2005.
- [11] T. A. Cruse and F. J. Rizzo. A direct formulation and numerical solution of the general transient elastodynamic problem, I. *Aust. J. Math. Anal. Appl.*, 22(1):244–259, 1968.
- [12] Lieven De Lathauwer, Bart De Moor, and Joos Vandewalle. A multilinear singular value decomposition. *SIAM J. Matrix Anal. A.*, 21(4):1253–1278, 2000. doi: 10.1137/S0895479896305696. URL <https://doi.org/10.1137/S0895479896305696>.
- [13] Simon Dirckx, Daan Huybrechs, and Karl Meerbergen. Frequency extraction for bem matrices arising from the 3d scalar helmholtz equation. *SIAM J. Sci. Comput.*, 44(5):B1282–B1311, 2022. doi: 10.1137/20M1382957. URL <https://doi.org/10.1137/20M1382957>.
- [14] M. G. Duffy. Quadrature over a pyramid or cube of integrands with a singularity at a vertex. *SIAM J. Numer. Anal.*, 19(6):1260–1262, 1982.
- [15] A. A. Ergin, B. Shanker, and E. Michielssen. Fast evaluation of three-dimensional transient wave fields using diagonal translation operators. *J. Comput. Phys.*, 146(1):157–180, 1998. doi: 10.1006/jcph.1998.5908.
- [16] S. Erichsen and S. A. Sauter. Efficient automatic quadrature in 3-d Galerkin BEM. *Comput. Methods Appl. Mech. Engrg.*, 157(3–4):215–224, 1998.
- [17] L. Greengard and V. Rokhlin. A new version of the Fast Multipole Method for the Laplace equation in three dimensions. *Acta Num.*, 6:229–269, 1997.
- [18] V. D. Kupradze, T. G. Gegelia, M. O. Basheleishvili, and T. V. Burchuladze. *Three-Dimensional Problems of the Mathematical Theory of Elasticity and Thermoelasticity*, volume 25 of *Applied Mathematics and Mechanics*. North-Holland, Amsterdam New York Oxford, 1979.

- [19] Michael Leitner and Martin Schanz. Generalized convolution quadrature based boundary element method for uncoupled thermoelasticity. *Mech Syst Signal Pr*, 150:107234, 2021. ISSN 0888-3270. doi: <https://doi.org/10.1016/j.ymsp.2020.107234>. URL <http://www.sciencedirect.com/science/article/pii/S0888327020306208>.
- [20] M. Lopez-Fernandez and S. Sauter. Generalized convolution quadrature with variable time stepping. *IMA J. of Numer. Anal.*, 33(4):1156–1175, 2013. doi: 10.1093/imanum/drs034.
- [21] M. Lopez-Fernandez and S. Sauter. Generalized convolution quadrature with variable time stepping. part II: Algorithm and numerical results. *Appl. Num. Math.*, 94:88–105, 2015.
- [22] María López-Fernández and Stefan Sauter. Generalized convolution quadrature based on Runge-Kutta methods. *Numer. Math.*, 133(4):743–779, 2016. doi: 10.1007/s00211-015-0761-2.
- [23] C. Lubich. Convolution quadrature and discretized operational calculus. I. *Numer. Math.*, 52(2):129–145, 1988.
- [24] C. Lubich. Convolution quadrature and discretized operational calculus. II. *Numer. Math.*, 52(4):413–425, 1988.
- [25] W. J. Mansur. *A Time-Stepping Technique to Solve Wave Propagation Problems Using the Boundary Element Method*. Phd thesis, University of Southampton, 1983.
- [26] V. Mantič. A new formula for the C-matrix in the somigliana identity. *J. Elasticity*, 33:191–201, 1993.
- [27] M. Messner and M. Schanz. An accelerated symmetric time-domain boundary element formulation for elasticity. *Eng. Anal. Bound. Elem.*, 34(11):944–955, 2010. doi: 10.1016/j.enganabound.2010.06.007.
- [28] I. V. Oseledets, D. V. Savostianov, and E. E. Tyrtyshnikov. Tucker dimensionality reduction of three-dimensional arrays in linear time. *SIAM J. Matrix Anal. A.*, 30(3):939–956, 2008. doi: 10.1137/060655894. URL <https://doi.org/10.1137/060655894>.
- [29] Y. Otani, T. Takahashi, and N. Nishimura. A fast boundary integral equation method for elastodynamics in time domain and its parallelisation. In M. Schanz and O. Steinbach, editors, *Boundary Element Analysis: Mathematical Aspects and Applications*, volume 29 of *Lecture Notes in Applied and Computational Mechanics*, pages 161–185. Springer-Verlag, Berlin Heidelberg, 2007.
- [30] A. Peirce and E. Siebrits. Stability analysis and design of time-stepping schemes for general elastodynamic boundary element models. *Int. J. Numer. Methods. Engrg.*, 40(2):319–342, 1997. doi: 10.1002/(SICI)1097-0207(19970130)40:2%3C319::AID-NME67%3E3.0.CO;2-I.
- [31] S. Sauter and A. Veit. Retarded boundary integral equations on the sphere: Exact and numerical solution. *IMA J. of Numer. Anal.*, 34(2):675–699, 2013.
- [32] S.A. Sauter and M. Schanz. Convolution quadrature for the wave equation with impedance boundary conditions. *J. Comput. Phys.*, 334:442–459, 2017. ISSN 0021-9991. doi: <http://dx.doi.org/10.1016/j.jcp.2017.01.013>. URL [//www.sciencedirect.com/science/article/pii/S0021999117300232](http://www.sciencedirect.com/science/article/pii/S0021999117300232).
- [33] F.-J. Sayas. *Retarded Potentials and Time Domain Boundary Integral Equations: A Road Map*, volume 50 of *Springer Series in Computational Mathematics*. Springer, Cham, 2016. doi: 10.1007/978-3-319-26645-9.

- [34] M. Schanz. *Wave Propagation in Viscoelastic and Poroelastic Continua: A Boundary Element Approach*, volume 2 of *Lecture Notes in Applied Mechanics*. Springer-Verlag, Berlin, Heidelberg, New York, 2001. doi: 10.1007/978-3-540-44575-3.
- [35] M. Schanz. On a reformulated convolution quadrature based boundary element method. *CMES Comput. Model. Eng. Sci.*, 58(2):109–128, 2010. doi: 10.3970/cmes.2010.058.109.
- [36] M. Schanz and H. Antes. A new visco- and elastodynamic time domain boundary element formulation. *Comput. Mech.*, 20(5):452–459, 1997. doi: 10.1007/s004660050265.
- [37] Martin Schanz. Realizations of the generalized adaptive cross approximation in an acoustic time domain boundary element method. *Proc. Appl. Math. Mech.*, 23(2):e202300024, 2023. doi: <https://doi.org/10.1002/pamm.202300024>. URL <https://onlinelibrary.wiley.com/doi/abs/10.1002/pamm.202300024>.
- [38] Martin Schanz, Wenjing Ye, and Jinyou Xiao. Comparison of the convolution quadrature method and enhanced inverse FFT with application in elastodynamic boundary element method. *Comput. Mech.*, 57(4):523–536, 2015. ISSN 0178-7675. doi: 10.1007/s00466-015-1237-z. URL <http://dx.doi.org/10.1007/s00466-015-1237-z>.
- [39] Daniel Seibel. Boundary element methods for the wave equation based on hierarchical matrices and adaptive cross approximation. *Numer. Math.*, 150(2):629–670, 2022. doi: 10.1007/s00211-021-01259-8. URL <https://doi.org/10.1007/s00211-021-01259-8>.
- [40] O. Steinbach. *Numerical Approximation Methods for Elliptic Boundary Value Problems*. Springer, 2008.
- [41] T. Takahashi, N. Nishimura, and S. Kobayashi. A fast BIEM for three-dimensional elastodynamics in time domain. *Eng. Anal. Bound. Elem.*, 28(2):165–180, 2004. Erratum in EABEM, 28, 165–180, 2004.
- [42] Ledyard R. Tucker. Some mathematical notes on three-mode factor analysis. *Psychometrika*, 31(3):279–311, 1966. doi: 10.1007/BF02289464. URL <https://doi.org/10.1007/BF02289464>.